INSTITUTE OF PHYSICS PUBLISHING JOURNAL OF PHYSICS: CONDENSED MATTER

J. Phys.: Condens. Matter **13** (2001) 6687–6706 PII: S0953-8984(01)22602-2

Fröhlich modes in porous III–V semiconductors

A Sarua[1], J Monecke[1], G Irmer[1], I M Tiginyanu[2,3], G Gärtner[4] and H L Hartnagel[5]

[1] Institut für Theoretische Physik, TU Bergakademie Freiberg, Bernhard-von-Cotta-Strasse 4, D-09596 Freiberg, Germany
[2] Department of Electrical Engineering and Computer Science, The University of Michigan, 1301 Beal Avenue, Ann Arbor, MI 48109-2122, USA
[3] Institute of Applied Physics, Technical University of Moldova, Boulevard Stefan cel Mare 168, MD-2004 Chisinau, Moldova
[4] Institut für Experimentelle Physik, TU Bergakademie Freiberg, Silbermannstrasse 1, D-09596 Freiberg, Germany
[5] Institut für Hochfrequenztechnik, TU Darmstadt, Merckstrasse 25, D-64283 Darmstadt, Germany

E-mail: sarua@physik.tu-freiberg.de

Received 7 March 2001, in final form 15 May 2001
Published 19 July 2001
Online at stacks.iop.org/JPhysCM/13/6687

Abstract

Porous GaP, InP and GaAs structures fabricated by MeV ion-implantation-assisted electrochemical etching were investigated by Raman and Fourier transform infrared spectroscopy. Fröhlich modes in the frequency gap between the transverse optical and longitudinal optical frequencies were observed and their longitudinal–transverse splitting was established. The frequency-dependent optical properties in the infrared region were calculated using a dielectric function derived on the basis of an appropriate two-dimensional effective-medium theory. The theoretical reflectance spectra are found to be in good agreement with the experimental ones and the predicted coupled Fröhlich–plasmon modes for conducting samples were observed experimentally. The wavelength used in Raman measurements did not fulfil the requirements of effective-medium theory, but the resulting spectra could be explained at least qualitatively by taking into account the diffuse scattering.

1. Introduction

Increasing attention has been paid in recent years to the study of the properties inherent to porous materials. In addition to porous silicon, widely investigated by a variety of different means [1, 2], porous III–V semiconductor compounds have aroused increasing interest [3–9] due to their potential applications in the field of electronics and photonics [10].

Optical investigations, such as Raman, infrared and luminescence spectroscopy, allow one to analyse these materials in a non-destructive way with high resolution and high sensitivity. Complemented by electrical measurements, they provide knowledge of fundamental properties necessary for possible device applications.

Porous GaP (por-GaP) layers and free-standing membranes proved to be excellent materials to use to study the peculiarities inherent to porous III–V semiconductor compounds. Recent progress in the fabrication of por-GaP by electrochemical etching allows one to control and to reproduce properties of the porous structures such as the morphology and basic electrical parameters in a desired way [11–14]. An enhanced optical response, new radiation and scattering properties and Fröhlich modes have already been reported for several porous III–V semiconductors [15–21].

Unlike in these works, we perform here a comparative study of Fröhlich modes [22] in both the infrared reflectance and Raman spectra of porous structures obtained by electrochemical etching of n-type GaP, InP and GaAs crystals. Fröhlich modes are of dielectric origin and occur in heterogeneous materials composed of at least one polar substance (not in the case of porous Si). The properties of the Fröhlich modes strongly depend on the morphology (i.e. symmetry, structural geometry, effective size etc) and on the properties of the constituents [23–26]. The analysis of these modes allows the characterization of the porous structure by the comparison of experimental results with theoretical calculations based on an effective-medium theory (EMT).

The longitudinal–transverse splitting of a Fröhlich mode in a porous polar material was first observed by Danishevskii *et al* [27] and by MacMillan *et al* in the infrared reflectance spectra of porous 6H-SiC layers [28]. A theoretical explanation of the results of the latter work was reported in terms of effective-medium expressions for the dielectric function based on the assumption that the structure can be described as built up from spheres using two different Maxwell-Garnett models [29]: the Bruggeman [30] and the Sheng [31] models.

In a recent work by Spanier and Herman [32] the infrared spectra of porous SiC are interpreted on the basis of a so-called hybrid dielectric function obtained as a combination of different 3D expressions. However, a model with spheres as building blocks cannot adequately describe most porous structures produced by electrochemical etching.

In this work we interpret the experimental spectra using a two-dimensional (2D) effective dielectric function, which describes the morphology of the porous structures as an interpolation between two boundary cases: cylindrical voids in the semiconducting matrix (large material concentration) and a skeleton of intercrossing semiconductor plates (large void concentration).

The morphology of the porous structures fabricated by electrochemical etching of III–V semiconductor materials depends mainly on the doping level of the initial material and on the crystal orientation for given etching conditions [3,4,33,34]. In the case of infrared reflectance measurements the light wavelength is much larger than the resulting structure dimensions and, hence, the porous structure can be considered as a homogeneous material for which effective-medium theories apply. In the case of Raman scattering the wavelength of the light inside the materials used is not much larger than the average structural dimensions, resulting in strong diffuse scattering. In this case effective-medium theories are not strictly applicable, in general.

We show that the Raman spectra can be described at least qualitatively by considering the porous crystal as a uniaxial one and taking into account the resulting angular distributions of excitations corresponding to the different light paths inside the porous structure due to diffuse scattering.

2. Effective-medium theory

2.1. The effective dielectric function

If the light wavelength λ is much larger than the characteristic structure dimensions L, porous semiconductors can be described as homogeneous materials and, in the range of IR frequencies, a quasi-static effective-medium theory can be applied to obtain an effective dielectric function. Parallel cylindrical pores in the Z-direction (see figure 1) which are randomly distributed in the XY-plane reduce the cubic symmetry of the bulk semiconductor to a uniaxial one. The cubic point group T_d is changed due to the loss of the threefold rotation axis $\langle 111\rangle$ to D_{2d} in the case of a (100) surface and due to the loss of the fourfold inversion axis $\langle 100\rangle$ to C_{3v} in the case of a (111)-oriented surface. In both cases the effective dielectric function becomes a tensor:

$$\tilde{\varepsilon}(\omega) = \begin{pmatrix} \varepsilon_\perp(\omega) & 0 & 0 \\ 0 & \varepsilon_\perp(\omega) & 0 \\ 0 & 0 & \varepsilon_\parallel(\omega) \end{pmatrix}. \tag{1}$$

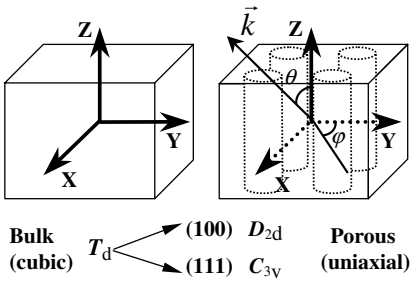

Figure 1. A schematic picture of the porous structure with parallel vertical cylindrical pores in a cubic crystal matrix. θ denotes the angle between the wavevector $\boldsymbol{k}$ of an excitation and the pore direction $\boldsymbol{Z}$.

For the electric field component parallel to the pores, $\varepsilon_\parallel(\omega)$ is given exactly by the upper Wiener limit [35]

$$\varepsilon_\parallel(\omega) = c\varepsilon(\omega) + (1-c)\varepsilon_0 \tag{2}$$

where ε_0 is the dielectric constant of air (filling the pores) and $\varepsilon(\omega)$ is the dielectric function of the semiconducting skeleton with relative volume concentration c, which is given in the IR region in the semi-insulating case by

$$\varepsilon(\omega) = \varepsilon_\infty \left[1 + \frac{\omega_{LO}^2 - \omega_{TO}^2}{\omega_{TO}^2 - \omega^2 - \mathrm{i}\omega\gamma} \right]. \tag{3}$$

In the limit of a few independent cylindrical pores ($c \to 1$) with the electric field perpendicular to the pore direction ($\boldsymbol{E} \perp \boldsymbol{Z}$ in figure 1), $\varepsilon_\perp(\omega)$ is given by

$$\varepsilon_\perp(\omega) = \frac{c\varepsilon(\omega) + (1-c)\varepsilon_0\langle E\rangle_2/\langle E\rangle_1}{c + (1-c)\langle E\rangle_2/\langle E\rangle_1} \tag{4}$$

with

$$\frac{\langle E\rangle_2}{\langle E\rangle_1} = \frac{\varepsilon(\omega)}{\varepsilon(\omega) + n(\varepsilon_0 - \varepsilon(\omega))} \tag{5}$$

and the depolarization factor $n = \frac{1}{2}$, where $\langle E\rangle_1$ and $\langle E\rangle_2$ denote spatial averages of the electric field components in the plane XY over the semiconductor and pore volumes, respectively.

In the opposite limit of vanishing relative concentration ($c \to 0$), we describe the walls of the remaining skeleton as semiconducting plates with normals randomly distributed in the XY-plane. In the case of one plate in an air matrix we get

$$\frac{\langle E\rangle_1}{\langle E\rangle_2} = \frac{\varepsilon_0}{\varepsilon_0 + n_i(\varepsilon(\omega) - \varepsilon_0)} \tag{6}$$

with $n_1 = 1$ for fields parallel to the plate normal and $n_2 = 0$ for fields perpendicular to the plate normal. Averaging over all angles φ ($\varphi \in [0, 2\pi]$) leads to

$$\frac{\langle E\rangle_1}{\langle E\rangle_2} = \frac{1}{2}\left[1 + \frac{\varepsilon_0}{\varepsilon(\omega)}\right] = \frac{\varepsilon_0 + \varepsilon(\omega)}{2\varepsilon(\omega)}. \tag{7}$$

Equation (4) together with either equation (5) or (7) leads to the same expression:

$$\varepsilon_\perp(\omega) = \varepsilon(\omega)\frac{(2-c)\varepsilon_0 + c\varepsilon(\omega)}{c\varepsilon_0 + (2-c)\varepsilon(\omega)}. \tag{8}$$

Equation (8), being correct in both limits $c \to 0$ and $c \to 1$ for the structure considered, can be taken as a suitable approximation for the entire range of c-values, $c \in [0, 1]$.

Any dielectric function has to obey the Bergman spectral representation [36].

With the definitions

$$s = \frac{1}{1 - \varepsilon(\omega)/\varepsilon_0} \tag{9}$$

and

$$F(s) = 1 - \frac{\varepsilon_\perp(\omega)}{\varepsilon_0} \tag{10}$$

we obtain from equation (8) the spectral representation

$$F(s) = \frac{A}{s} + \int_0^1 \frac{g(x)}{s - x}\,\mathrm{d}x \tag{11}$$

with

$$A = c/(2-c) \qquad g(x) = B\delta(x - s_0)$$
$$s_0 = 1 - \frac{c}{2} \qquad B = \frac{c(1-c)}{2-c}.$$

The exact relations [36]

$$A + \int_0^1 g(x)\,\mathrm{d}x = c \tag{12}$$

and

$$\int_0^1 x g(x)\,\mathrm{d}x = \frac{1}{2}c(1-c) \tag{13}$$

in the two-dimensional case, as realized for our samples, are both fulfilled.

$A \neq 0$ for all c-values, which reflects the fact that the percolation threshold of the semiconducting skeleton is given by $c = 0$, the plates forming the skeleton being connected for all $c \neq 0$.

In a two-dimensional case the Keller theorem [37] states that

$$\varepsilon_\perp(\varepsilon_0, \varepsilon(\omega), c)\varepsilon_\perp(\varepsilon(\omega), \varepsilon_0, c) = \varepsilon_0\varepsilon(\omega) \tag{14}$$

where $\varepsilon_\perp(\varepsilon_0, \varepsilon(\omega), c)$ is the dielectric function given in our case by equation (8) and $\varepsilon_\perp(\varepsilon(\omega), \varepsilon_0, c)$ is a dielectric function with $\varepsilon(\omega)$ and ε_0 interchanged (an interpolation between

cylindrical semiconductor columns and randomly oriented air layers with c being the air concentration). Equation (8) fulfils this requirement, too.

From equations (3) and (8) it is easy to calculate the reflectivity (normal incidence):

$$R(\omega) = \frac{(n(\omega) - 1)^2 + \kappa(\omega)^2}{(n(\omega) + 1)^2 + \kappa(\omega)^2} \tag{15}$$

with

$$n(\omega) = \frac{1}{\sqrt{2}}\sqrt{\mathrm{Re}(\varepsilon_\perp(\omega)) + \sqrt{\mathrm{Re}^2(\varepsilon_\perp(\omega)) + \mathrm{Im}^2(\varepsilon_\perp(\omega))}} \tag{16}$$

and

$$\kappa(\omega) = \frac{1}{\sqrt{2}}\sqrt{-\mathrm{Re}(\varepsilon_\perp(\omega)) + \sqrt{\mathrm{Re}^2(\varepsilon_\perp(\omega)) + \mathrm{Im}^2(\varepsilon_\perp(\omega))}}. \tag{17}$$

The result is a two-band reflectance spectrum as shown in figure 2 for vanishing phonon damping γ.

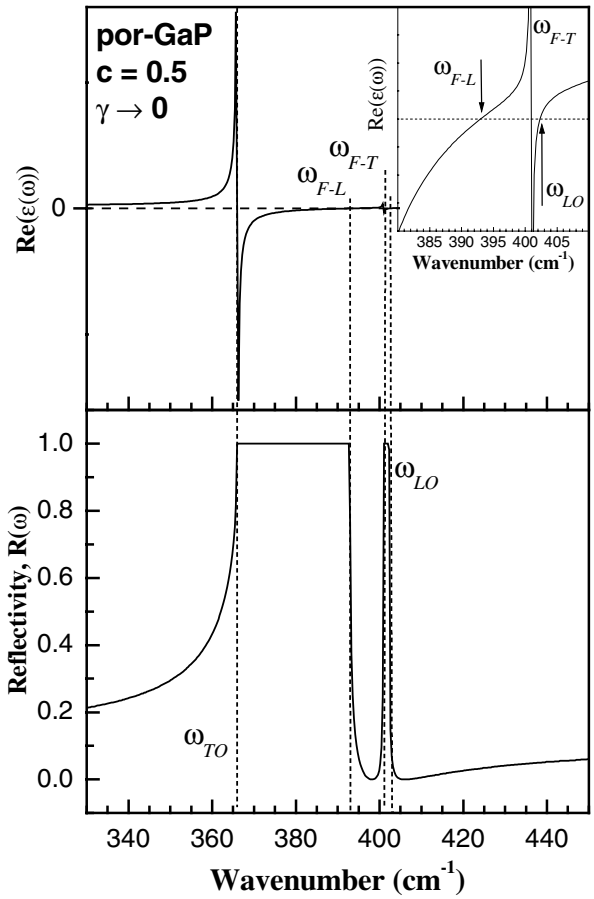

Figure 2. The calculated real part of the dielectric function and the reflectivity of por-GaP with semiconductor concentration $c = 0.5$ and phonon damping $\gamma \to 0$. The inset shows $\mathrm{Re}(\varepsilon(\omega))$ in the frequency range of total reflectance.

The pole in $\varepsilon_\perp(\omega)$ at $\varepsilon_0 + \varepsilon(\omega) = 0$ for $c \to 1$ is a Fröhlich mode [22], the resonance mode of one circular pore in the semiconducting matrix in the frequency gap between ω_{LO} and ω_{TO}. Being a pole it is of transverse (T) character. In addition to this mode, $\varepsilon_\perp(\omega)$ as given by equation (8) has a pole at the frequency ω_{TO}. Poles of any dielectric function should always alternate with zeros, longitudinal (L) modes, in the sequence T–L–T–L with increasing frequency. We therefore expect a L–T splitting of the Fröhlich mode with decreasing c, its L part being below the T one.

Both longitudinal and transverse Fröhlich modes can easily be calculated from equation (8) and are shown for all c and $\gamma \to 0$ in figure 3. The frequency range between the longitudinal and transverse Fröhlich modes (F–L and F–T) corresponds to the new reflectivity gap in figure 2.

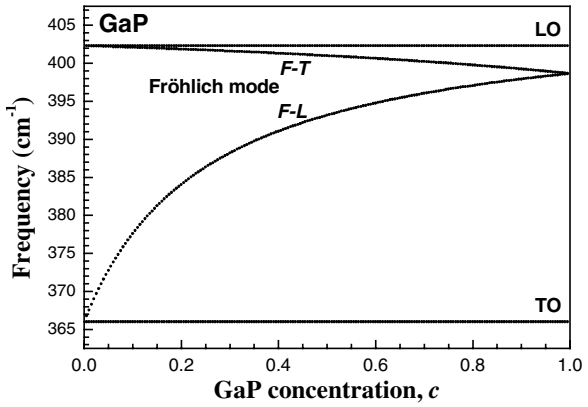

Figure 3. Calculated frequencies of TO-phonon, LO-phonon and Fröhlich modes for vanishing phonon damping ($\gamma \to 0$).

In uniaxial crystals, ordinary and extraordinary (angle-dependent) excitations exist. In the absence of damping the corresponding frequencies are given by (see e.g. [38])

$$\varepsilon_\perp(\omega) = \infty \tag{18}$$

and

$$\varepsilon_\perp(\omega)\sin^2\theta + \varepsilon_\parallel(\omega)\cos^2\theta = 0 \tag{19}$$

where θ is the angle between the pore direction ($\boldsymbol{Z}$) and the wavevector $\boldsymbol{k}$ of the excitation (see figure 1) giving rise to Raman scattering (θ is *not* the angle between the pore direction and the electric field). For $\gamma \neq 0$ the corresponding Raman intensities in the IR region are proportional (at least in the case of one dominant scattering mechanism) to

$$I_{\mathrm{o}} \sim \mathrm{Im}(\varepsilon_\perp(\omega)) \tag{20}$$

and

$$I_{\mathrm{eo}} \sim \mathrm{Im}\left(-\frac{1}{\varepsilon_\perp(\omega)\sin^2\theta + \varepsilon_\parallel(\omega)\cos^2\theta}\right) \tag{21}$$

where the subscripts 'o' and 'eo' stand for ordinary and extraordinary, respectively.

$\varepsilon_\parallel(\omega)$ as given by equation (2) has (for $\gamma = 0$) the same pole at $\omega = \omega_{\mathrm{TO}}$ as $\varepsilon(\omega)$, and a zero, which depends on c. It can be rewritten as

$$\varepsilon_\parallel(\omega) = \varepsilon_\infty^{(1)}\frac{\omega^2 - \omega_1^2(c)}{\omega^2 - \omega_{\mathrm{TO}}^2} \tag{22}$$

with

$$\varepsilon_\infty^{(1)} = (1-c)\varepsilon_0 + c\varepsilon_\infty \tag{23}$$

and

$$\omega_1^2(c) = \frac{(1-c)\varepsilon_0\omega_{\mathrm{TO}}^2 + c\varepsilon_\infty\omega_{\mathrm{LO}}^2}{(1-c)\varepsilon_0 + c\varepsilon_\infty}. \tag{24}$$

$\varepsilon_\perp(\omega)$ as given by equation (8) is a product of $\varepsilon(\omega)$ with a pole at $\omega = \omega_{\mathrm{TO}}$ and a zero at $\omega = \omega_{\mathrm{LO}}$ times a factor with one additional pole and one additional zero corresponding to the F–T and F–L modes. Hence, it can be written as

$$\varepsilon_\perp(\omega) = \varepsilon_\infty^{(2)} \frac{\omega^2 - \omega_{\mathrm{LO}}^2}{\omega^2 - \omega_{\mathrm{TO}}^2} \frac{\omega^2 - \omega_2^2(c)}{\omega^2 - \omega_3^2(c)} \tag{25}$$

with

$$\varepsilon_\infty^{(2)} = \frac{(2-c)\varepsilon_0 + c\varepsilon_\infty}{(2-c)\varepsilon_\infty + c\varepsilon_0}\varepsilon_\infty \tag{26}$$

and

$$\omega_2^2(c) = \frac{(2-c)\varepsilon_0\omega_{\mathrm{TO}}^2 + c\varepsilon_\infty\omega_{\mathrm{LO}}^2}{(2-c)\varepsilon_0 + c\varepsilon_\infty} \tag{27}$$

$$\omega_3^2(c) = \frac{(2-c)\varepsilon_\infty\omega_{\mathrm{LO}}^2 + c\varepsilon_0\omega_{\mathrm{TO}}^2}{(2-c)\varepsilon_\infty + c\varepsilon_0}. \tag{28}$$

The ordinary part of the Raman scattering according to equations (8) and (18) gives rise to two peaks at $\omega = \omega_{\mathrm{TO}}$ and $\omega = \omega_3(c)$, these being the ordinary excitations of TO-phonon and transverse Fröhlich mode character, respectively.

The extraordinary part of the Raman scattering gives rise to two additional peaks near the solutions of

$$\varepsilon_\infty^{(1)}(\omega^2 - \omega_1^2(c))(\omega^2 - \omega_3^2(c))\cos^2\theta + \varepsilon_\infty^{(2)}(\omega^2 - \omega_{\mathrm{LO}}^2(c))(\omega^2 - \omega_2^2(c))\sin^2\theta = 0. \tag{29}$$

These peaks depend on the angle θ and correspond to the extraordinary LO-phonon and the longitudinal Fröhlich excitations. The calculated angular dependences of all modes are displayed in figure 4 for different GaP concentrations.

2.2. Plasmons

In the presence of free carriers inside the semiconductor skeleton, the dielectric function $\varepsilon(\omega)$ has to be complemented by a plasmon part. This contribution was chosen in the form of the simple Drude expression because it is expected that other approximations (e.g. the EMT approach, the neglect of the formation of depletion layers within the skeleton [11] etc) would negate any benefits to be derived from more sophisticated treatments. Hence, we replace equation (3) by

$$\varepsilon(\omega) = \varepsilon_\infty\left[1 + \frac{\omega_{\mathrm{LO}}^2 - \omega_{\mathrm{TO}}^2}{\omega_{\mathrm{TO}}^2 - \omega^2 - \mathrm{i}\omega\gamma} - \frac{\omega_{\mathrm{pl}}^2}{\omega(\omega + \mathrm{i}\Gamma)}\right] \tag{30}$$

with

$$\omega_{\mathrm{pl}} = \sqrt{\frac{N_e e^2}{\varepsilon_\infty m^*}} \tag{31}$$

and the plasmon damping coefficient

$$\Gamma = \frac{e}{\mu m^*}. \tag{32}$$

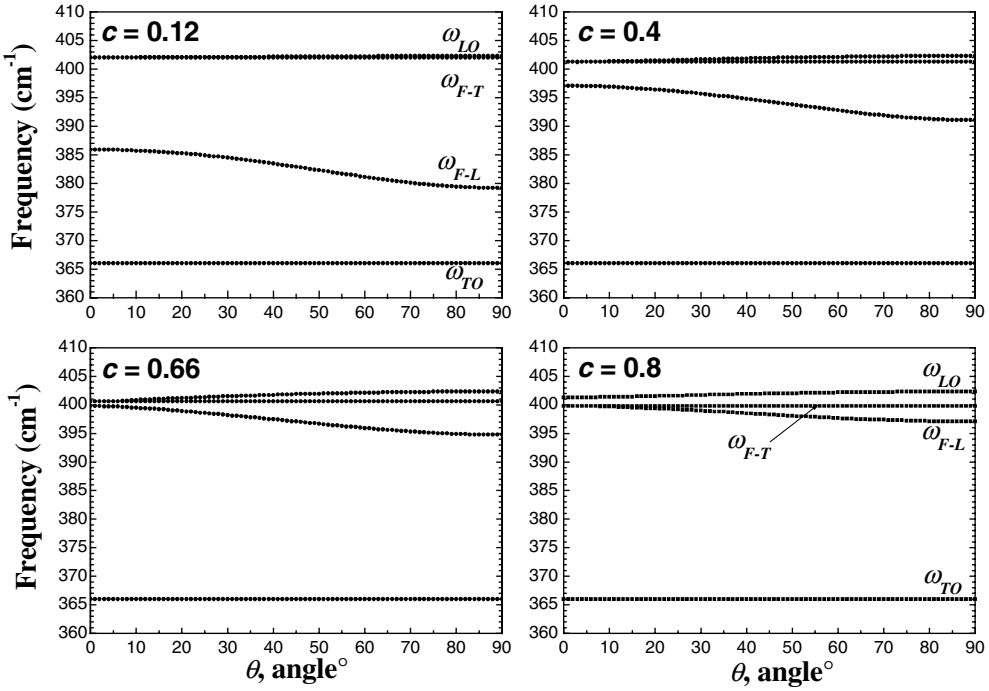

Figure 4. The calculated angular dependences of excitations in uniaxial por-GaP for vanishing phonon damping ($\gamma \to 0$).

The transverse and longitudinal modes resulting from equation (8) as functions of the free-carrier concentration N_e (keeping c fixed and choosing $\gamma, \Gamma \to 0$) are given for InP in figure 5.

In addition to the coupled LO-phonon–plasmon modes L_+ and L_- of the bulk material, coupled Fröhlich–plasmon modes (F–T_+, F–T_-, F–L_+ and F–L_-) appear in the porous structures. These modes depend on the free-carrier concentration N_e and on the carrier mobility. The unusual coupling between plasmons and transverse Fröhlich modes can be understood as follows: for $c \to 0$ the transverse Fröhlich mode is fixed at the position of the LO phonon and for $c \to 1$ it is fixed at the position of the longitudinal Fröhlich mode (see figure 3). Longitudinal optical modes undergo frequency shifts with N_e and, therefore, the transverse Fröhlich mode is shifted together with them.

3. Experimental details

Porous layers were obtained by electrochemical etching of n-type LEC-grown crystalline substrates in aqueous acidic solutions (see table 1).

In order to initiate the etching process the samples were implanted with 5 MeV Kr ions with a dose of 3×10^{10} cm^{-2}. The etching was carried out in darkness for 30 minutes. Subsequently the porous layers were detached from the substrate by lateral etching in order to obtain free-standing porous membranes as described in reference [34]. The process of etching is strongly influenced by the initial doping level of the substrate material, by the defect density on the surface and by the crystal orientation. In our case the pores exhibit a column-like shape, stretching into the sample perpendicularly to the initial crystal surface (see figure 6). The

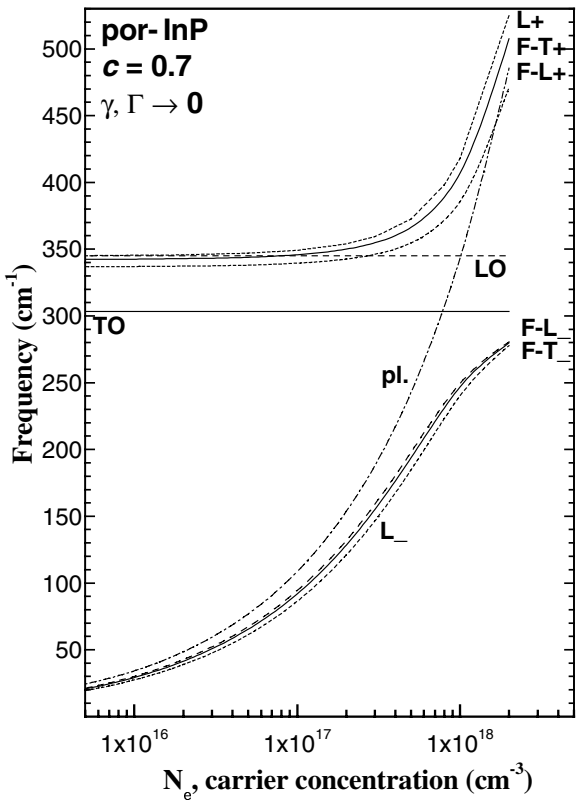

Figure 5. Calculated frequencies of LO-phonon (L_+ and L_-) and Fröhlich modes coupled with plasmons ('pl.') ($F–T_+$, $F–L_+$, $F–T_-$ and $F–L_-$). LO, TO and pl. denote the pure phonon and plasmon modes.

Table 1. Material data and etching conditions.

	n-GaP	n-InP	n-GaAs
Crystal orientation	100 111	100	100
Free-carrier concentration (cm^{-3}) at $T = 300$ K	5×10^{17} $(1–2) \times 10^{18}$	$(2–3) \times 10^{17}$	$(2–3) \times 10^{17}$
Etching solution	0.5M H_2SO_4	HCl	HCl
Current density (mA cm^{-3})	4–5	20	20
Etching time (min)	30	30	30

thickness of the remaining semiconductor skeleton walls L can be estimated to be nearly twice the thickness of the depletion layer $L \approx 2L_D$ [11]. The total thickness of the porous layers was approximately 50 μm in the case of por-GaP and 5–10 μm in the cases of por-GaAs and por-InP layers.

Micro-Raman measurements were performed using a Jobin-Yvon T64000 triple spectrometer equipped with a nitrogen-cooled CCD system. The spectra were acquired in nearly backscattering geometry with a spectral resolution less than 0.5 cm^{-1}. A cw Ar^+ laser

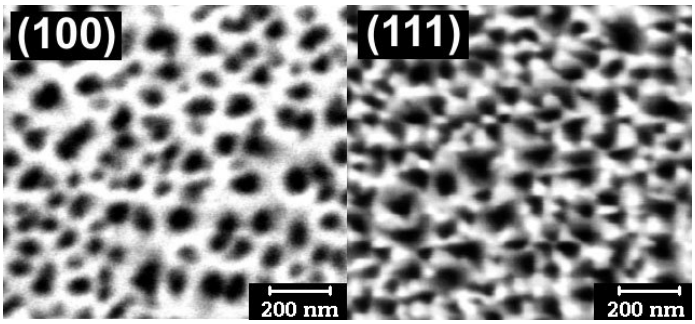

Figure 6. SEM micrographs of differently oriented GaP samples etched in aqueous acid solution (top view).

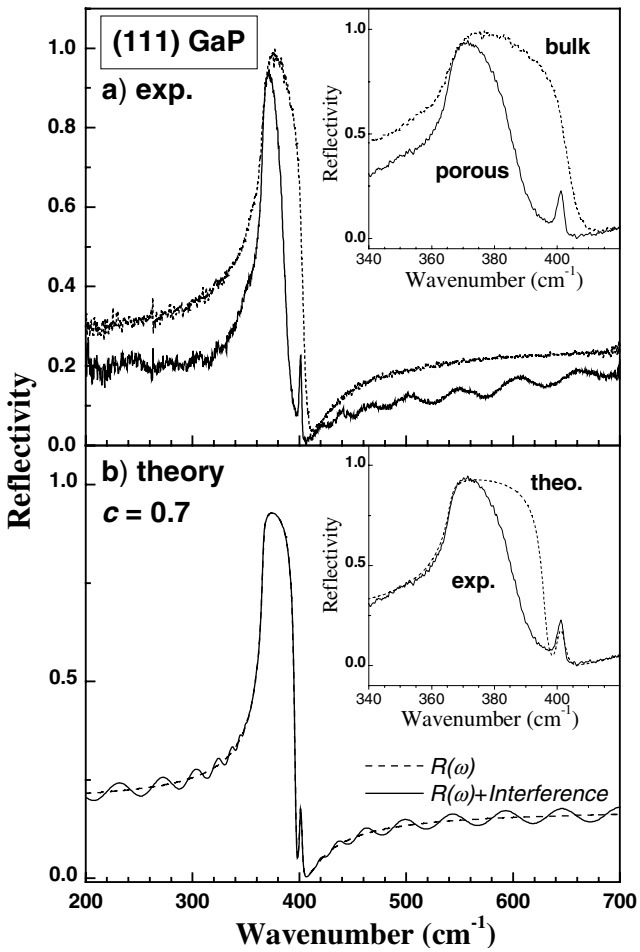

Figure 7. FTIR reflectance spectra of (111) GaP. (a) Measured at $T = 300$ K for a porous sample (solid) and for the bulk initial crystal (dashed) and (b) calculated from the effective dielectric function (8) for the semi-insulating skeleton with $c = 0.7$ and $\gamma = 1.5$ with (dashed) and without (solid) internal interferences inside the porous membrane. The inset shows the measured (solid) and theoretical (dashed) reflectivity in the frequency range of total reflectance.

(514.532 nm) and a Ti:sapphire laser working at 900 nm were used. In order to avoid thermal heating the laser power was limited to 1 mW in a spot with a diameter of about 1 μm. The measurements at low temperature (77 K) were carried out using a CryoVac set-up.

The Fourier transform infrared (FTIR) reflectance measurements were performed at room temperature using a Bruker IFS 133v Fourier transform spectrometer with maximal resolution of about 0.03 cm^{-1}. A reflectance set-up with the angle of incidence of 11° was used.

4. Experimental data

4.1. GaP

Examples of the room temperature FTIR reflectance spectra of por-GaP are displayed in figure 7 and figure 8. Instead of the one-band reflectance spectrum of bulk material, a two-band structure is observed. A Kramers–Kronig transformation (KKT) analysis allows one to obtain

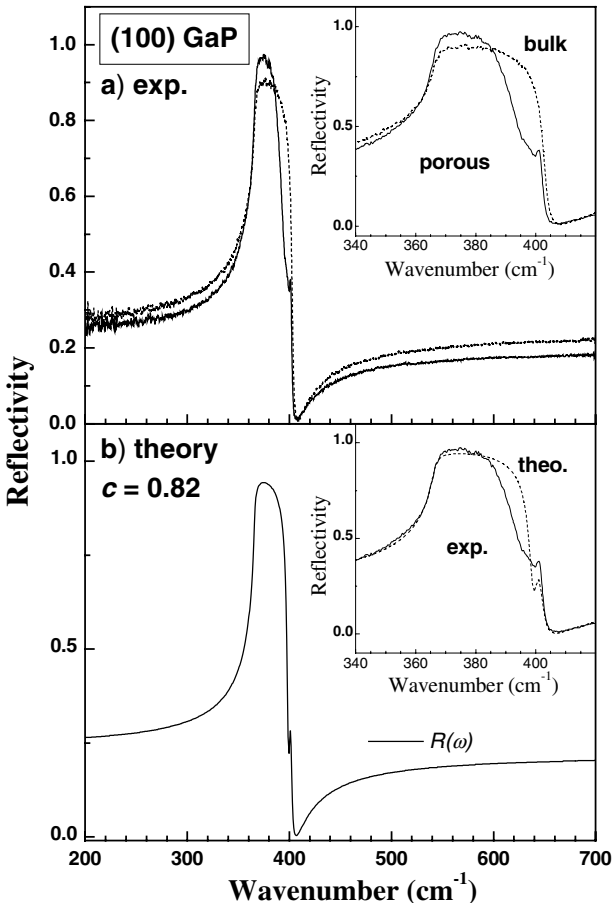

Figure 8. FTIR reflectance spectra of (100) GaP. (a) Measured at $T = 300$ K for a porous sample (solid) and for the bulk initial crystal (dashed) and (b) calculated from the effective dielectric function (8) for the semi-insulating skeleton with $c = 0.82$ and $\gamma = 1.5$ with (dashed) and without (solid) internal interferences inside the porous membrane. The inset shows the measured (solid) and theoretical (dashed) reflectivity in the frequency range of total reflectance.

the phonon frequencies. The wave-like features in the spectra of (111) GaP membranes are related to interference of the light with multiple reflections at the two boundaries of the porous membrane and were modelled within a three-layer model using the layer thickness and the angle of incidence known from the FTIR set-up as input parameters.

The Raman spectra of porous GaP samples, displayed in figure 9(a) and figure 10(a) together with those of the initial bulk material, show a breakdown of the symmetry selection rules.

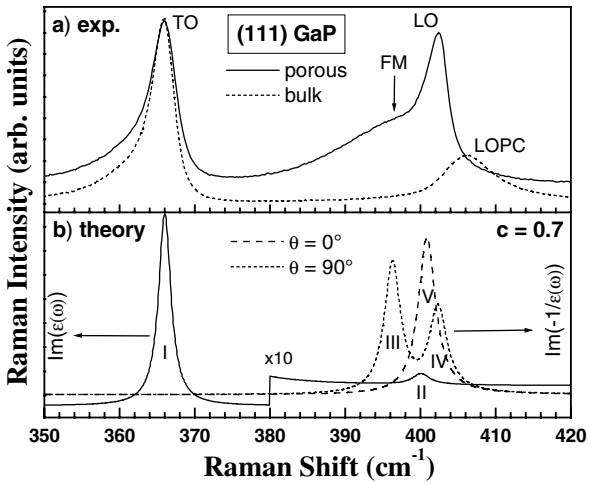

Figure 9. Raman spectra of (111) GaP. (a) Measured at $T = 300$ K (FM denotes the Fröhlich mode) and (b) calculated; the Roman numerals have the following meanings: I: TO; II: transverse Fröhlich; III: longitudinal Fröhlich; IV: LO; and V: extraordinary LO modes calculated from the effective dielectric function. Longitudinal modes (dashed) are given for $\theta = 0^\circ$ and 90°; transverse modes (solid) are angle independent.

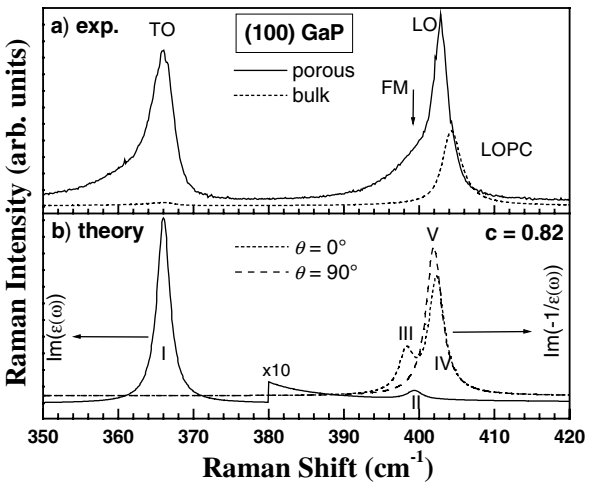

Figure 10. Raman spectra of (100) GaP. (a) Measured at $T = 300$ K (FM denotes the Fröhlich mode) and (b) calculated; the Roman numerals have the following meanings: I: TO; II: transverse Fröhlich; III: longitudinal Fröhlich; IV: LO; and V: extraordinary LO modes calculated from the effective dielectric function. Longitudinal modes (dashed) are given for $\theta = 0^\circ$ and 90°; transverse modes (solid) are angle independent.

Regardless of the crystal orientation, both the TO- and the LO-phonon modes occur at 366 cm^{-1} and 402.3 cm^{-1}, respectively, while for bulk (100)-oriented substrates only the LO phonon is allowed in backscattering geometry. The observation of the weak forbidden TO phonon in the bulk (100) samples is related to the crystal imperfection and/or to possible deviations from the true backscattering geometry. The LO-phonon–plasmon coupled (LOPC) modes of the doped bulk substrate are no longer observed in por-GaP samples. Additionally, the spectra of the porous samples exhibit a relatively broad band located between the TO- and LO-phonon modes. Its peak position was found to be 398.7 cm^{-1} and 399.3 cm^{-1} with full widths at half-maximum of 8–10 cm^{-1} for (100)- and (111)-oriented por-GaP, respectively.

4.2. InP and GaAs

Examples of the room temperature FTIR reflectance spectra of por-InP are given in figure 11(a). Similarly to the case for por-GaP, a two-band reflectance spectrum is observed. In the case

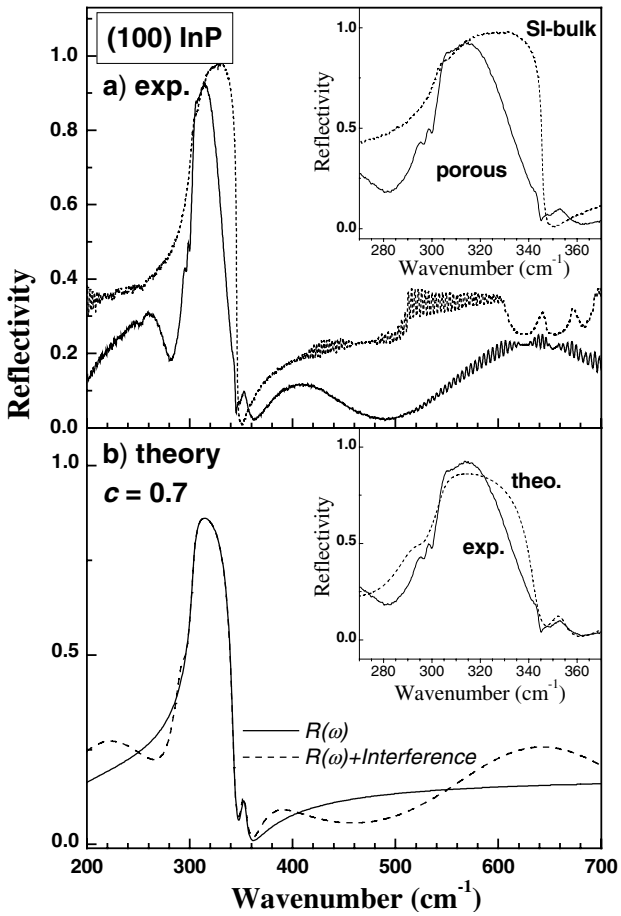

Figure 11. FTIR reflectance spectra of (100) InP. (a) Measured at $T = 300$ K for a porous sample (solid) and for a bulk semi-insulating crystal (dashed) and (b) calculated from the effective dielectric function (8) for $c = 0.7$, $\gamma = 1.5$, $N_e = 3 \times 10^{17}$ cm^{-3} and $\mu = 2500$ cm^2 V^{-1} s^{-1} with (dashed) and without (solid) internal interferences inside the porous sample.

of por-InP, the band position is affected by the interaction of the LO-phonon and the Fröhlich modes with plasmons inside the InP skeleton.

The Raman spectra of por-InP and por-GaAs were measured at 77 K. They are shown together with those of the initial bulk crystals in figure 12, figure 13 and figure 14. Unlike in the case for GaP, both branches of the LOPC mode, the L_+ and the L_- modes (together with a relatively weak LO mode from the depleted surface regions), are observed in the Raman spectra. Calculations using the experimental values of the peak positions and peak widths of the coupled modes allow one to estimate the free-carrier concentrations and mobilities inside the skeleton.

The experimental results are summarized in table 2.

Table 2. Phonon frequencies (in cm^{-1}) obtained from FTIR reflectance and Raman scattering measurements ($T = 300$ K). Data in the brackets are those for the corresponding bulk material.

	(100) por-GaP		(111) por-GaP		(100) por-InP		(100) por-GaAs
	FTIR	Raman	FTIR	Raman	FTIR	Raman*	Raman*
L_-	Not present				—	146.7 (148.2)	197.7 (203.3)
TO	366	366	366	366	303.7	303.7	273.5
F–L	398.5	399.3[a]	396.3	398.7[a]	343.4	349.7[a]	302.4[a]
F–T	399.5	399.3[a]	400.2	398.7[a]	350.9	349.7[a]	302.4[a]
LO	402.3	402.5	402.3	402.3	(345.5)	345.5	292.8
L_+	(402.8)	(405.2)	(406.3)	(406.4)	355.1	354.6 (354.8)	313.8 (315.4)

* Measured at $T = 77$ K.
[a] Only one Fröhlich mode was observed.

5. Discussion

5.1. GaP

The morphology of porous (100) GaP can be approximated by parallel cylindrical voids in the semiconductor matrix (randomly distributed in the XY-plane) as shown schematically in figure 1. In the case of (111) orientation the pores are rather of triangular shape. Such a morphology cannot be described by an analytical EMT expression, and more than one Fröhlich mode is expected, in general [39]. However, because only one mode could be resolved in the experiments (see figure 7–figure 10) we will apply the model of cylindrical pores as an approximation for this case, too.

The light wavelength used in the FTIR measurements is much larger than the average structure dimension. In this case the EMT approach can be applied. The measured FTIR reflectance spectra reflect well the behaviour predicted by the effective dielectric function. Due to an additional zero and an additional pole at ω_{FL} and ω_{FT}, respectively, a two-band reflectance spectrum appears. The energetic distance between these two bands is given by the L–T splitting of the Fröhlich modes and allows one to estimate the relative concentration c. The results of the EMT-based calculations for por-GaP samples are given in figure 7(b) and figure 8(b). They show satisfactory agreement with the spectra obtained experimentally. The difference between the calculated and the measured reflectance bands as regards the high-frequency shoulder can result from the scattering losses of the reflected signal (caused by e.g. surface roughness).

The Raman measurements on por-GaP show that porosity leads to a depleted GaP skeleton. Instead of the LOPC modes inherent to the doped bulk samples, the LO-phonon mode of pure

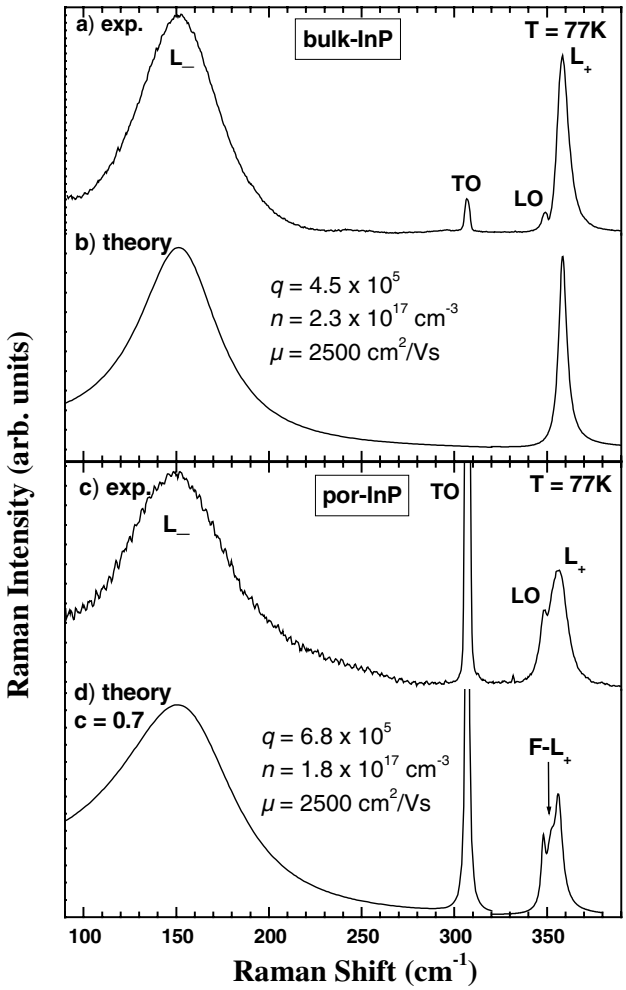

Figure 12. Raman spectra of bulk and porous (100) InP. (a), (c) Measured at $T = 77$ K and (b), (d) calculated from the dielectric function (Lindhard–Mermin theory). F–L_+, L_+ and L_- denote coupled modes.

GaP is observed at 402.3 cm^{-1} (see figure 9(a) and figure 10(a)). An additional broad structure between the TO and LO phonons is interpreted as being the Fröhlich mode. The Raman spectra calculated on the basis of the effective dielectric function (equation (8)) are shown together with the experimental ones in figure 9 and figure 10. The theory reproduces well the position of the Fröhlich mode, but its large bandwidth cannot be explained in a simple way.

The average dimensions of the por-GaP structures are of the same order as the wavelength of the light exciting the Raman spectra. The resulting diffuse scattering leads to the violation of the symmetry selection rules, i.e. the TO phonon can be observed in the Raman spectra regardless of the surface orientation.

Additionally, in true backscattering geometry ($\theta = 0^\circ$) only three modes (I, II and V in figure 9(b) and figure 10(b)) are expected in the Raman spectra for a given c-value (see also figure 4). The observation of the strong Fröhlich mode (III in figure 9 and figure 10) becomes possible only at θ near 90°.

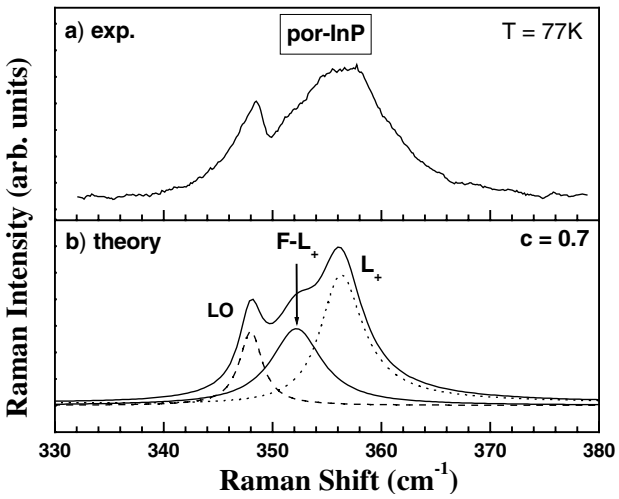

Figure 13. Raman spectra of porous (100) InP. (a) Measured at $T = 77$ K and (b) calculated from the dielectric function (Lindhard–Mermin theory). F–L_+ and L_+ denote coupled modes.

One has to note that in the case of $\lambda \approx L$ any EMT-based approach is not strictly valid. Due to the lack of a suitable theory we will nevertheless apply EMT as a first approximation, but taking into account different angles of incidence θ within the porous structure due to diffuse scattering.

Because the extraordinary excitations are angle dependent (see figure 4), an effective broadening of the Fröhlich modes results in this way. However, the full width of the experimentally observed Fröhlich modes is larger than that resulting just from the angular dependence. This additional broadening of the Fröhlich modes could be due to a c-value distribution in real samples (e.g. due to misalignment of pore directions and shapes) and perhaps to an influence of surface oxidation ($\varepsilon_{\text{oxid}} \geqslant \varepsilon_0$). These effects can hardly be determined in a quantitative way by the experimental means employed and need further consideration.

5.2. InP and GaAs

Similarly to the case for por-GaP, a two-band structure is observed in the FTIR reflectance spectra of porous InP (see figure 11). However, the high-frequency shoulder of the band at higher frequencies appears at larger wavenumbers than that given by the LO-phonon position of semi-insulating (SI) InP. This shift is caused by the free carriers present inside the InP skeleton. The high-frequency band is formed by coupled L_+ and F–T_+ modes, whereas the low-frequency band is enclosed by the TO-phonon and coupled F–L_+ modes. The frequency shifts of the coupled modes obtained from equations (18), (19) and (30) are given in figure 5. In the absence of damping there occur, beside the L_- part of the LOPC modes, coupled F–L_- and F–T_- modes below the TO phonon, too. Taking into account actual damping constants, they are not expected to be observable due to their weak intensities and their large bandwidths, and we could not observe them in our samples.

In the case of por-GaAs we used the data obtained by Raman measurements in order to calculate the FTIR reflectance spectra from the effective dielectric function. According to the theoretical simulation the relatively small TO–LO splitting of bulk phonon modes together with the large phonon damping do not result in a pronounced reflectance band between the F–T and

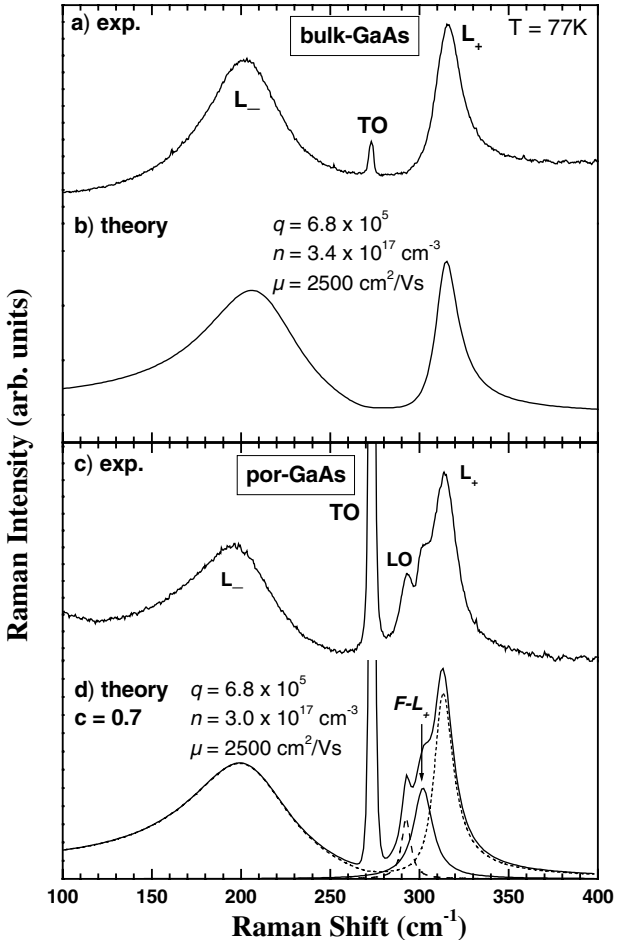

Figure 14. Raman spectra of bulk and porous (100) GaAs. (a), (c) Measured at $T = 77$ K and (b), (d) calculated from the dielectric function (Lindhard–Mermin theory). F–L_+, L_+ and L_- denote coupled modes.

LO (or L_+) mode (see figure 15). Accordingly we did not succeed in finding unambiguously the two-band spectra in the case of our por-GaAs samples.

The Raman spectra of por-InP and por-GaAs show similar modifications to those observed in the case of por-GaP. Diffuse scattering of the incident light inside the porous structures gives rise to the observation of strong TO-phonon modes, which are forbidden for the bulk material (see figure 12 and figure 14). A broad Fröhlich band between the bulk phonons is also observed. The frequencies of the LO-phonon and the Fröhlich modes are influenced by the interaction with plasmons. This gives rise to coupled modes in the spectra as discussed above.

The free-carrier concentrations and their mobilities inside the semiconducting skeleton can be estimated by analysis of the LOPC modes, as was demonstrated for bulk samples [40]. We performed the fitting of the coupled L_+ and L_- modes for both porous and bulk substances (see figure 12–figure 14). In order to take into account the $\boldsymbol{q}$-dependence of the dielectric function and to fit the line shape of the coupled optical modes in the measured spectra, the Lindhard–Mermin approach [41] was chosen. The charge-carrier concentrations and mobilities

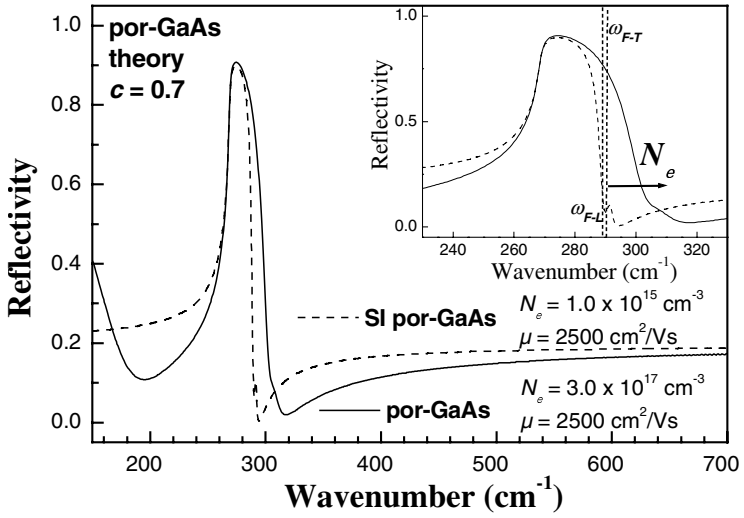

Figure 15. FTIR reflectance spectra of porous GaAs calculated from the effective dielectric function. Dashed: for semi-insulating por-GaAs; solid: for the conductive skeleton of por-GaAs, using the data obtained from the Raman spectrum ($N_e = 3 \times 10^{17}$ cm^{-3} and $\mu = 2500$ cm^2 V^{-1} s^{-1}). The inset shows the same in the region of total reflectance. The direction of the frequency shift of Fröhlich modes (F–L and F–T) with increasing free-carrier concentration (N_e) is shown by the arrow.

obtained in this way were used to calculate the frequencies of the coupled Fröhlich modes from equation (29) (see figure 13 and figure 14). The LO-phonon frequency of the depleted layer was taken to be that of the SI bulk material. The fits performed show a good agreement for por-InP and por-GaAs samples.

6. Conclusions

Using electrochemical etching techniques combined with high-energy ion implantation, it is possible to produce porous III–V semiconductors with well-defined average structure dimensions (skeleton thickness) of about $L \approx 2L_D$, where L_D is the depletion layer thickness corresponding to the bulk charge-carrier concentration N_e, and with a relative concentration c of the semiconducting material of about $c \approx 0.7$–0.8.

In the IR frequency region the essential supposition of effective-medium theories, $\lambda \gg L$, is justified and the FTIR reflectance spectra can be described on the basis of a suitable 2D EMT. The L–T splitting of the Fröhlich mode predicted by the theory for $0 < c < 1$ was observed and coupled Fröhlich–plasmon modes could be detected experimentally in the case of por-InP. The unusual coupling of a transverse mode with plasmons could be explained.

In the case of Raman scattering measurements the wavelength of the laser light employed inside the samples is not much larger than the typical structure dimensions. In this case EMTs are not strictly applicable, in general. However, the experimental spectra proved the existence of a Fröhlich mode in the frequency gap between the bulk TO and LO phonons. The observed large full width of this mode could at least partially be explained by the excitation of angle-dependent extraordinary modes by diffuse scattered light. In the case of conducting porous samples the coupled Fröhlich–plasmon modes were found in the Raman spectra in good agreement with theoretical predictions.

In order to prove unambiguously the uniaxial symmetry of porous III–V semiconductors by optical means, it is necessary for the condition $\lambda \gg L$ to be fulfilled. In the case of Raman measurements, this could be achieved by a sufficient increase of the excitation wavelength with the disadvantage of a low scattering efficiency and/or by scaling down the structure dimensions.

Acknowledgment

This work was supported by the German Research Society (DFG).

References

[1] Canham L T 1990 *Appl. Phys. Lett.* **57** 1046
[2] Cullis A G, Canham L T and Calcott P D J 1997 *J. Appl. Phys.* **82** 909
[3] Erne B H, Vanmaekelbergh D and Kelly J J 1996 *J. Electrochem. Soc.* **143** 1137
Erne B H, Vanmaekelbergh D and Kelly J J 1996 *J. Electrochem. Soc.* **143** 305
[4] Schmuki P, Fraser J, Vitus C M, Graham M J and Isaacs H S 1996 *J. Electrochem. Soc.* **143** 3316
[5] Tiginyanu I M, Irmer G, Monecke J and Hartnagel H L 1997 *Phys. Rev.* B **55** 6739
[6] Takizawa T, Arai S and Nakahara M 1994 *Japan. J. Appl. Phys.* **33** L643
[7] Tiginyanu I M, Schwab C, Grob J-J, Prévot B, Hartnagel H L, Vogt A, Irmer G and Monecke J 1997 *Appl. Phys. Lett.* **71** 3829
[8] Lockwood D J, Schmuki P, Labbe H J and Fraser J 1999 *Physica* E **4** 102
[9] Anedda A, Serpi A, Karavanski V A, Tiginyanu I M and Ichizli V M 1995 *Appl. Phys. Lett.* **67** 3316
[10] Bell J 1999 *Opto Laser Europe* **60** 31
[11] Sarua A, Tiginyanu I M, Ursaki V V, Irmer G, Monecke J and Hartnagel H L 1999 *Solid State Commun.* **112** 581
[12] Tiginyanu I M, Irmer G, Monecke J, Hartnagel H L, Vogt A, Schwab C and Grob J-J 1999 *Proc. Mater. Res. Soc. Symp. (Boston, MA)* vol 546, ed L T Canham, M J Sailor, K Tanaka and Ch-Ch Tsai (Warrendale, PA: Materials Research Society) p 99
[13] Tiginyanu I M and Hartnagel H L 1999 *GaAs '99 Conf. Proc. (Munich, 4–5 October 1999)* (London: Miller Freeman) pp 194–9
[14] Sarua A, Irmer G, Monecke J, Tiginyanu I M, Schwab C, Grob J-J and Hartnagel H L 2000 *J. Appl. Phys.* **88** 7006
[15] Schuurmans J P, Vanmaekelbergh D, van de Lagermaat J and Lagendijk A 1999 *Science* **284** 141
[16] Tiginyanu I M, Ursaki V V, Raptis Y S, Stergiou V, Anastassakis E, Hartnagel H L, Vogt A, Prévot B and Schwab C 1999 *Phys. Status Solidi* b **211** 281
[17] Tiginyanu I M, Kravetsky I V, Makovsky G and Hartnagel H L 1999 *Phys. Status Solidi* a **175** R5
[18] Kiriyama K, Ushiyama K, Ohbora K, Miyamoto Y and Takeda S 1998 *Phys. Rev.* B **58** 1103
[19] da Silva S W, Galazerani J C, Lubyshev D I and Basmaji P 1998 *J. Phys.: Condens. Matter* **10** 9687
[20] Denisov V N, Marvin B N and Karavanskii V A 1999 *Phys. Lett.* A **259** 62
[21] Sarua A, Gärtner G, Irmer G, Monecke J, Tiginyanu I M and Hartnagel H L 2000 *Proc. 2nd Int. Conf. on Porous Semiconductors—Science and Technology (PSST-2000) (Madrid); Phys. Status Solidi* a **182** 207
[22] Fröhlich H 1949 *Theory of Dielectrics* (Oxford: Clarendon)
[23] Ruppin R and Englman R 1970 *Rep. Prog. Phys.* **33** 144
[24] Monecke J 1994 *J. Phys.: Condens. Matter* **6** 907
[25] Monecke J 1989 *Phys. Status Solidi* b **154** 805
[26] Monecke J 1989 *Phys. Status Solidi* b **155** 437
[27] Danishevskii A M, Shuman V B, Rogachev A Yu and Ivanov P A 1995 *Semiconductors* **29** 1106
[28] MacMillan M F, Devaty R P, Choyke W J, Goldstein D R, Spanier J E and Kurtz A D 1996 *J. Appl. Phys.* **80** 2412
[29] Maxwell-Garnett J C 1904 *Phil. Trans. R. Soc.* A **203** 385
Maxwell-Garnett J C 1906 *Phil. Trans. R. Soc.* A **205** 237
[30] Bruggeman D A G 1935 *Ann. Phys., Lpz.* **24** 636
[31] Sheng P 1980 *Phys. Rev. Lett.* **45** 60
[32] Spanier J E and Herman I P 2000 *Phys. Rev.* B **61** 10 437
[33] Oskam G, Natarajan A, Searson P C and Ross F M 1997 *Appl. Surf. Sci.* **119** 160
[34] Miao J, Tiginyanu I M, Hartnagel H L, Irmer G, Monecke J and Weiss B 1997 *Appl. Phys. Lett.* **70** 491

[35] Wiener O 1912 *Abh. Math.-Phys. Kl. Königl. Sachs. Ges.* **32** 509
[36] Bergman D J 1978 *Phys. Rep.* **43** 377
[37] Keller J B 1963 *J. Appl. Phys.* **34** 991
Keller J B 1964 *J. Math. Phys.* **5** 548
[38] Agranovich V M and Kravtsov V E 1985 *Solid State Commun.* **55** 85
[39] Fuchs R 1975 *Phys. Rev.* B **11** 1732
[40] Irmer G, Wenzel M and Monecke J 1997 *Phys. Rev.* B **56** 9524 and references therein
[41] Mermin N D 1970 *Phys. Rev.* B **1** 2362